Model Predictive Control Method With Variable Weight Coefficients for Switched Reluctance Motor Under Different Operations

Shoujun Song, *Senior Member, IEEE*, Xinyu Bai, Guilin Sun, Chaoyang Liu, Lefei Ge, *Member, IEEE*, Ningfei Jiao, *Member, IEEE*, and Weiguo Liu, *Senior Member, IEEE*

***Abstract*—In the propulsion and electrical systems of more-electric aircraft (MEA), the switched reluctance motor (SRM) is regarded as one of the key motor topologies due to its simple structure, high-temperature tolerance, wide speed range, and strong fault tolerance. Due to the inherent torque ripple, its application range is limited. Model predictive control (MPC), with its multivariable optimization capability, has been widely applied in torque ripple suppression and efficiency improvement of SRM. Nevertheless, conventional MPC typically adopts fixed weighting coefficients in the cost function, which limits its applicability under varying operations. To address this issue, this article proposes a fuzzy-control-based variable-weight MPC (FCMPC) strategy. By constructing a fuzzy inference system based on a load torque observer, the proposed method dynamically adjusts the weighting coefficient in the cost function according to the motor's operating state, thereby achieving adaptive optimization of the control strategy. The method exhibits excellent performance in both dynamic and steady-state conditions, significantly enhancing the generality and control performance of MPC under various operating conditions. It is particularly suitable for MEA applications that demand high control precision and fast dynamic response.**

***Index Terms*—Fuzzy control strategy, model predictive control (MPC), multicondition operation, switched reluctance motor (SRM), variable weighting coefficients.**

NOMENCLATURE

$\theta_{\text{ph}}, \psi_{\text{ph}}$	Rotor position and flux linkage.
$i_{\text{ph}}, u_{\text{ph}}$	Phase current and voltage.
R_{ph}	Phase resistance.
$\omega, \hat{\omega}$	Actual and estimated speed.
$\tilde{\omega}$	Speed estimation error.
Δt	Control period.
$U_{\text{dc}}, I_{\text{dc}}$	DC bus voltage and current.
S_k	Excitation state $(-1, 0, 1)$.
J_q	Cost function.
q_t	Weighting coefficients of torque.
q_i	Weighting coefficients of current.
$T_{e,p}, T_{\text{ref}}$	Estimated and reference torque.
T_{em}, T_L	Electromagnetic and load torque.
$T_{\max}, T_{\min}$	Maximum and minimum torque.
T_{avg}	Average torque.
k_T, η	Torque ripple and motor efficiency.
$\mathcal{S}$	Search set of current weighting coefficients.
$I(q_i)$	Current fluctuation terms.
$k_T^{\min}$	Minimum torque ripple.
$I_{\min}$	Minimum current.
$\mathcal{Q}_T, \mathcal{Q}_I$	Torque and current constraint set.
$\mathcal{Q}$	Feasible set.
I_{ref}	Reference current energy.
F_{q_i}	Fuzzy set of the current weighting factor.
F_{T_L}	Fuzzy set of the load torque.
F_{ω_r}	Fuzzy set of the rotor speed.
R_i	ith fuzzy rule.
D	Viscous damping coefficient.
J	Moment of inertia.
k	Sliding-mode gain.
$\hat{T}_L'$	Unfiltered estimated load torque.
$\hat{T}_L$	Filtered estimated load torque.
ω_c	Cutoff frequency of the low-pass filter.
s	Laplace operator.

Received 21 May 2025; revised 13 October 2025 and 28 November 2025; accepted 21 December 2025. Date of publication 30 December 2025; date of current version 20 March 2026. This work was supported in part by the National Natural Science Foundation of China under Grant 52277067, in part by the Aeronautical Science Foundation of China under Grant 20220040053001, in part by the Shaanxi Provincial Science Foundation for Distinguished Young Scholars under Grant 2023-JC-JQ44, in part by the Dreams Foundation of Jianghuai Advance Technology Center under Grant 2023-ZM01J001, and in part by the research projects of AVIC Shaanxi Aero Electric Company, Ltd. under Grant JSJSHT2312280030. Recommended for publication by Associate Editor F. D. Freijedo. *(Corresponding author: Lefei Ge.)*

Shoujun Song, Xinyu Bai, Guilin Sun, Lefei Ge, Ningfei Jiao, and Weiguo Liu are with the Department of Electrical Engineering, School of Automation, Northwestern Polytechnical University, Xi'an 710072, China (e-mail: sunnyway@nwpu.edu.cn; xinyu_bai@mail.nwpu.edu.cn; wonderful_u@mail.nwpu.edu.cn; lge@nwpu.edu.cn; jiaoningfei@nwpu.edu.cn; lwglll@nwpu.edu.cn).

Chaoyang Liu is with Platform and Module Development Department, Changan Automobile, Chongqing 400020, China (e-mail: liuchaoyang@mail.nwpu.edu.cn).

Color versions of one or more figures in this article are available at https://doi.org/10.1109/TPEL.2025.3649351.

Digital Object Identifier 10.1109/TPEL.2025.3649351

I. INTRODUCTION

WITH the growth of the global economy, escalating energy consumption has led to massive carbon emissions, posing serious challenges to the ecological environment [1]. Among various transportation modes, the aviation sector has emerged as a major contributor to carbon emissions due to its heavy reliance on a stable fuel supply to ensure flight safety and sustained operation at cruising altitude [2].

To achieve efficient, low-carbon and sustainable flight, more-all electric aircraft have become key research focuses in industry and academia [3]. As more-electric aircraft (MEA) technologies continue to evolve, aircraft power systems are shifting from conventional centralized architectures toward highly integrated and high power density electrical frameworks [4].

Among the key enabling technologies of MEA [5], the embedded starter/generator (ESG) integrates engine starting and power generation functions through a directly coupled configuration with the engine. This technology not only enhances system reliability but also greatly reduces volume and weight, thereby strongly supporting the development of highly integrated and lightweight aircraft electrical systems [6].

The switched reluctance motor (SRM) offers excellent bidirectional operating capability [7] and is particularly well-suited for high-temperature environments due to its simple structure, which lacks windings and permanent magnets on the rotor [8]. As a result, SRM reluctance starter/generator systems are considered an ideal candidate for ESG applications [9]. In addition, SRM exhibits a wide constant power speed range and strong fault-tolerant performance [10], [11]. These features align closely with the high-performance requirements of electric drive systems in MEA, positioning SRM as a strong contender in the future of aircraft electrification [12].

However, several critical challenges remain to be addressed for SRM-based ESG systems. The inherently high torque ripple may cause shaft damage and induce blade resonance in the aircraft engine, posing potential safety risks to the system [13]. Meanwhile, the high ambient temperature and poor cooling conditions inside the engine lead to significant energy losses in the starter/generator, thereby reducing overall system efficiency [14].

Therefore, a variety of advanced control strategies have been proposed to enhance the dynamic response of the SRM, improve its torque output characteristics, and further reduce energy losses [15], [16]. Although the conventional chopping current control is simple to implement, its limited control frequency hinders precise current tracking and delays the response, making it unsuitable for high-performance applications [17].

In recent years, model predictive control (MPC) has become an important research focus in SRM control due to its excellent dynamic response and multiobjective optimization capability [18]. In [19], a model predictive current control method for six-phase SRM was proposed based on an improved Lehuy model, combined with a sliding-mode disturbance observer to effectively suppress performance degradation caused by parameter mismatches. In [20], a torque sharing function was integrated with pulsewidth modulation control signals, where a linear polynomial fitting method was adopted to expand predictive data, achieving accurate reference torque tracking and effective torque ripple suppression. Furthermore, Han et al. [21] addressed the difficulty of obtaining accurate SRM mathematical models by proposing a current difference-based model-free predictive current control method, which requires only phase currents at two consecutive sampling points to achieve efficient control.

However, conventional MPC adopts fixed weighting factors, making it difficult to adapt to the variation of objective priorities under different operating conditions, and thus, it cannot maintain optimal performance across various scenarios. As highlighted in [22], the selection of weighting factors remains a key challenge restricting the performance of MPC.

To eliminate the dependence on predefined weighting factors, various approaches have been proposed. Elmorshedy et al. [23] constructed a weighting-factor-free cost function based on the maximum thrust per ampere strategy, reducing the computational complexity of linear induction machine control and improving efficiency. Wang et al. [24] presented an improved cascaded finite-set MPC scheme that balances dynamic performance and steady-state accuracy while avoiding complex weighting factor tuning. Xie et al. [25] achieved multiobjective optimization without weighting parameters through cost function decomposition and sorting algorithms. Zhang et al. [26] reconstructed the cost function using direct voltage-vector selection, thereby completely eliminating weighting factors and enhancing system robustness.

In terms of weighting factor optimization, a variety of intelligent and self-tuning methods have also been proposed. Wang et al. [27] employed an improved particle swarm optimization algorithm for automatic tuning of weighting factors, reducing torque ripple and switching frequency. Yao et al. [28] combined artificial neural network (ANN) with genetic algorithms to obtain optimal weighting factors through offline training. Guazzelli et al. [29] applied nondominated sorting genetic algorithm II to optimize weighting factors, achieving a tradeoff among torque ripple, flux ripple, and switching frequency. Liu et al. [30] designed weighting factors algebraically and incorporated integral terms into the cost function to eliminate steady-state error.

As summarized above, there is currently no unified method for determining weighting coefficients in MPC, and research specifically focused on SRM remains limited. To address this gap, this article proposes a fuzzy-control-based variable-weight MPC (FCMPC) strategy that enables adaptive adjustment of the weighting coefficient, significantly enhancing the adaptability and engineering applicability of MPC under complex operations.

The main contributions of this article are as follows.

1) The control performance of MPC with different weighting coefficients under various operations is analyzed, and the selection patterns of optimal coefficients are obtained through simulation.
2) A fuzzy controller is introduced to enable online adjustment of weighting coefficients, enhancing the dynamic multiobjective optimization capability of MPC.
3) A load torque observer based on sliding-mode control theory is designed. The fuzzy controller takes the real-time rotor speed and the observed load torque as inputs to output the corresponding adaptive weighting coefficient, enabling MPC to adjust control priorities according to the current operations.

The rest of this article is organized as follows. Section II introduces the control principle of MPC and constructs the associated cost function. Section III analyzes the selection rules for weighting coefficients under different operations, and based on this, proposes the FCMPC strategy. It also presents the design

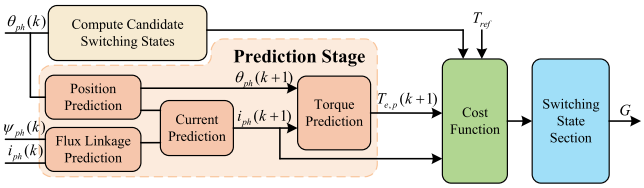

Fig. 1. Schematic diagram of MPC.

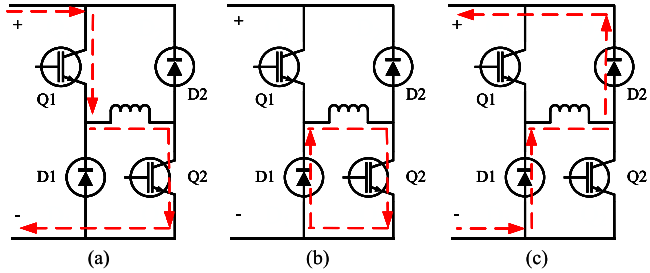

Fig. 2. Operating states of the power converter. (a) Magnetization. (b) Freewheeling. (c) Demagnetization.

of a sliding-mode-based load torque observer used to provide torque input to the fuzzy controller. Section IV validates the proposed method through semiphysical experimental testing. Finally, Section V concludes this article.

II. Principle of Predictive Control for SRM

Predictive control, based on currently available measurement data and a predictive model, calculates the system output under various input conditions, and then selects the input that best meets the control objectives for the next control cycle.

A. System Structure

The schematic diagram of MPC system is illustrated in Fig. 1. The MPC module primarily consists of four components: candidate switching state calculation, predictive stage, cost function construction, and switching state selection. The system inputs include $\theta_{\text{ph}}(k)$, $\psi_{\text{ph}}(k)$, $i_{\text{ph}}(k)$, and T_{ref}.

B. Predictive Computation

The predictive computation mainly consists of four parts: position prediction, flux linkage prediction, current prediction, and torque prediction.

1) Position Prediction: The predicted rotor position is obtained from the current rotor position and angular velocity as

$$\theta_{\text{ph}}(k+1) = \theta_{\text{ph}}(k) + \omega \Delta t. \tag{1}$$

2) Flux Linkage Prediction: The discrete-time expression for flux linkage prediction is derived using Euler's formula as

$$\psi_{\text{ph}}(k+1) = \psi_{\text{ph}}(k) + \left(S_k U_{\text{dc}} - i_{\text{ph}}(k) R_{\text{ph}}\right) \Delta t. \tag{2}$$

The phase flux linkage $\psi_{\text{ph}}(k)$ is computed from $\psi_{\text{ph}} = \int (u_{\text{ph}} - R_{\text{ph}} i_{\text{ph}})\, dt$. Based on all possible switching states of each phase winding, the predicted flux linkage values at time step $k+1$ are calculated.

S_k represents the candidate switching state of each phase winding and is defined as

$$S_k = \begin{cases} +1, & \text{magnetization} \\ 0, & \text{freewheeling} \\ -1, & \text{demagnetization.} \end{cases} \tag{3}$$

The current paths under different switching states are shown in Fig. 2, where (a) denotes the magnetization mode with both switches turned-ON, (b) the freewheeling mode with one switch turned-ON, and (c) the demagnetization mode with both switches turned-OFF. The red arrows indicate the current direction and illustrate the variation of energy flow under different operating states.

3) Current Prediction: After obtaining the predicted rotor position $\theta_{\text{ph}}(k+1)$ and flux linkage $\psi_{\text{ph}}(k+1)$, the predicted current value $i_{\text{ph}}(k+1)$ at the next time step can be retrieved using a two-dimensional position–flux linkage–current lookup table [31].

4) Torque Prediction: Similar to the current prediction process, once the predicted position $\theta_{\text{ph}}(k+1)$ and current $i_{\text{ph}}(k+1)$ are known, the predicted torque $T_{e,p}(k+1)$ at the next time step can be obtained using a two-dimensional position-current-torque lookup table.

C. Cost Function Construction

MPC performs optimization over the predicted switching state combinations through a cost function, with priority given to torque tracking while also considering current optimization to suppress torque ripple and improve overall system performance. In summary, based on the dual control objectives of torque and current, the conventional MPC cost function for the SRM is formulated as

$$J_q = q_t \left(\sum_{p=1}^{3} T_{e,p}(k+1) - T_{\text{ref}} \right)^2 + q_i \sum_{\text{ph}=1}^{3} \left| i_{\text{ph}}(k+1) \right|^2. \tag{4}$$

q_t and q_i are used to coordinate the two optimization objectives of torque and current by adjusting their relative priorities within the MPC framework, thereby enabling the generation of more optimal switching signals. The controller selects the most appropriate switching state for the power converter based on the minimum value of the cost function. The impact of these weighting coefficients on control performance and their role in regulating control priorities will be discussed in the following section.

III. Proposed Variable Weighting Strategy

To address the limitations of fixed weighting coefficients in conventional SRM MPC, particularly the inability to dynamically balance torque tracking and current suppression under varying speed and load conditions, this article proposes a variable weighting factor strategy.

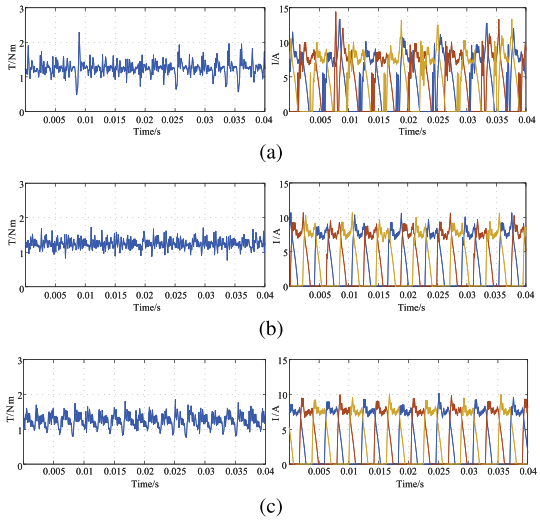

Fig. 3. Total torque and phase current under different weighting coefficients at 1200 r/min /1 N · m. (a) $q_i = 0$. (b) $q_i = 0.001$. (c) $q_i = 0.01$.

A. Study on Weighting Coefficients in MPC of SRM

This section investigates the selection method of weighting coefficients in conventional MPC for SRM, and analyzes the selection patterns of these coefficients under different operations through simulation.

1) Weighting Coefficient Setting in Traditional MPC: In SRM control, torque ripple suppression is the primary objective, while current optimization serves as a secondary goal. Due to the coupling between current and torque, a too low current weighting coefficient may cause waveform distortion and increased torque ripple. Therefore, it is essential to properly balance the weighting coefficients of torque and current to achieve optimal control performance.

This section presents an simulation analysis of weighting coefficient selection in the conventional MPC cost function, using the 1200 r/min/1 N · m operation as an example. By fixing the torque weighting coefficient $q_t = 1$ and varying the current weighting coefficient q_i among 0, 0.001, and 0.01, the control performance is evaluated to determine an appropriate order of magnitude for q_i. The torque ripple is calculated using the following equation:

$$k_T = \frac{T_{\max} - T_{\min}}{T_{\text{avg}}} \times 100\%. \tag{5}$$

The motor efficiency can be calculated using the following expression:

$$\eta = \frac{T_{\text{em}}\omega}{U_{\text{dc}} I_{\text{dc}}} \times 100\%. \tag{6}$$

The total torque simulation results and the corresponding current waveforms under the operation of 1200 r/min and 1 N · m for different current weighting coefficients are shown in Fig. 3.

When the current weighting coefficient is set to $q_i = 0$, the cost function neglects current constraints entirely, resulting in significant current spikes and increased torque ripple. With $q_i = 0.001$, the cost function properly accounts for current constraints, leading to a smoother current waveform and achieving a good balance between torque control and efficiency improvement. However, when $q_i = 0.01$, the cost function places excessive emphasis on current, a secondary control objective, which compromises torque tracking performance. Although a slight improvement in efficiency is observed, the torque ripple increases noticeably.

TABLE I
TORQUE RIPPLE AND EFFICIENCY UNDER DIFFERENT WEIGHTING COEFFICIENTS AT 1200 R/MIN/1N · M

q_i	k_T (%)	η (%)	q_i	k_T (%)	η (%)
0	145.9	61.0	0.006	66.0	68.2
0.001	83.3	66.6	0.007	72.6	68.3
0.002	79.3	66.9	0.008	84.0	68.0
0.003	76.6	67.2	0.009	88.0	68.4
0.004	70.3	67.8	0.010	89.0	68.5
0.005	66.4	68.2			

Based on the simulation results above, it can be concluded that the appropriate order of magnitude for the current weighting coefficient under the operation of 1200 r/min/1 N · m lies within the range of [0.001, 0.01]. To further determine the optimal coefficient for this condition, additional simulation were conducted with q_i confined to this interval. The corresponding simulation results of torque ripple and efficiency for each selected weighting coefficient within the range are summarized in Table I.

As shown in Table I, both the torque ripple and efficiency of the SRM vary with changes in the weighting coefficient. Within a reasonable range of magnitudes, the optimal selection of the weighting coefficient should primarily aim to minimize the torque ripple. According to the simulation results, when the weighting coefficient is set to $q_i = 0.005$ or $q_i = 0.006$, the SRM achieves the lowest torque ripple under the 1200 r/min/1 N · m operation. Under these coefficient values, the conventional MPC demonstrates relatively optimal control performance.

2) Performance Analysis of Conventional MPC Under Different Operations: The conventional MPC cost function adopts fixed weighting coefficients, resulting in constant control priorities that cannot adapt to changes in operations. To evaluate its performance under varying conditions, two representative operating points were selected: 1000 r/min at 2 N · m and 1200 r/min at 0.5 N · m. The simulation results for torque ripple and efficiency under different current weighting coefficients are presented in Fig. 4.

It can be observed that the variation of the q_i has a significant influence on torque ripple characteristics, as analyzed below. With the increase of the current weighting coefficient q_i, the torque ripple coefficient k_T first decreases and then increases, indicating that there exists an optimal q_i within a certain range that minimizes the torque ripple. When q_i is small, the controller emphasizes torque tracking, resulting in larger current fluctuations and higher torque ripple. As q_i increases, the current regulation capability is enhanced, and the torque ripple is significantly reduced. However, when q_i becomes excessively large, the controller oversuppresses current variation, limiting the torque response and causing the torque ripple to rise again. Meanwhile, the efficiency η changes little with q_i,

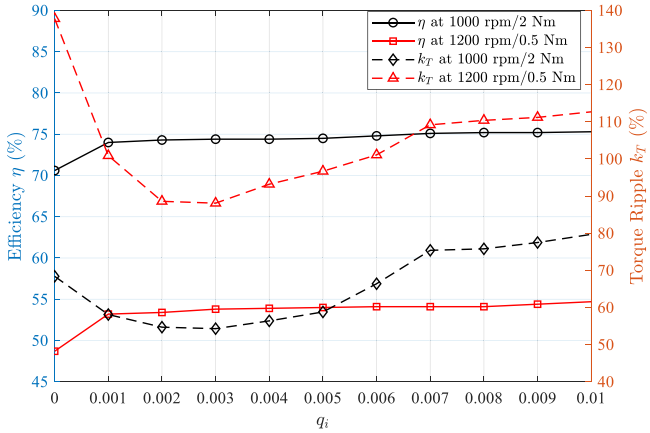

Fig. 4. Torque ripple and efficiency under different current weighting coefficients.

indicating that the weighting coefficient mainly affects torque ripple while having minimal influence on energy conversion efficiency. Therefore, the simulation results demonstrate that there exists an optimal tradeoff between torque smoothness and dynamic response. The conventional MPC with fixed weighting factors cannot maintain this balance under all operating conditions, which verifies the necessity of the proposed FCMPC fuzzy adaptive weighting mechanism.

3) Selection of MPC Weighting Coefficients for SRM: This section further investigates the selection rules of MPC weighting coefficients for SRM under various operations through simulation, serving as a data foundation for the variable-weighting MPC strategy proposed in the next section.

The motor speed is divided into nine levels ranging from 400 to 1200 r/min, and the load torque is set to five levels from 0.5 to 2.5 N · m. To reasonably determine the current weighting coefficient q_i under the condition of a fixed torque weighting $q_t = 1$, this study conducts an analysis based on the cost function (4). For each operating condition (ω, T_L), a weighting search set is defined as follows:

$$\mathcal{S} = \{\, q_i \mid q_i \in [0.001,\ 0.01],\ \Delta q_i = 0.001 \,\}. \tag{7}$$

For each candidate $q_i \in S$, the steady-state electromagnetic torque waveform is obtained, and the corresponding torque-ripple factor is computed from (5). The minimum torque ripple is then given by

$$k_T^{\min} = \min_{q_i \in S} k_T. \tag{8}$$

To ensure that the torque-ripple performance remains close to the optimum, a 5% relative tolerance band is adopted, and the constraint set of the weighting factors is defined as

$$\mathcal{Q}_T = \left\{ q_i \in S \,\middle|\, \frac{k_T - k_T^{\min}}{k_T^{\min}} \le 5\% \right\}. \tag{9}$$

For the current index, the global minimum current over the search set $\mathcal{S}$ is obtained as

$$I_{\min} = \min_{q_i \in S} I(q_i) = \min_{q_i \in S} q_i \sum_{p=1}^{3} \left| i_{\mathrm{ph}}(k+1) \right|^2. \tag{10}$$

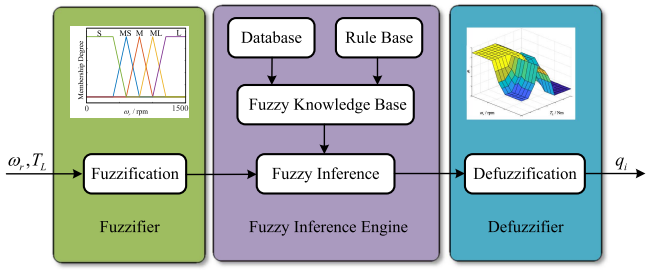

Fig. 5. Overall structure of the fuzzy control strategy.

Specifically, $I(q_i)$ denotes the current obtained at the corresponding operating condition when the current weighting factor is set to q_i. To avoid an increase in current while reducing the torque ripple, a relative tolerance of 0.5% is adopted, and the constraint set for the current constraint is defined as

$$\mathcal{Q}_I = \left\{ q_i \in S \,\middle|\, \frac{I(q_i) - I_{\min}}{I_{\min}} \le 0.5\% \right\}. \tag{11}$$

The feasible region is given by

$$\mathcal{Q} = \mathcal{Q}_T \cap \mathcal{Q}_I. \tag{12}$$

The optimal coefficient and feasible range are determined as

$$[q_i^{\min},\ q_i^{\max}] = [\min(\mathcal{Q}),\ \max(\mathcal{Q})]. \tag{13}$$

After repeating this process across all speed–load conditions, the global recommended range is summarized in Table II. The results reveal significant variation in the optimal q_i values across different operations. Due to the use of fixed weighting coefficients, conventional MPC struggles to maintain consistent control performance under diverse conditions. Therefore, to achieve high-performance SRM control across a wide range of operating states, it is essential to construct an MPC cost function with dynamic priority adjustment capability.

To address this challenge, the next section proposed an MPC strategy with fuzzy logic-based variable weighting to enable adaptive and optimized control performance for SRM under complex operations.

B. Fuzzy Control-Based Variable Weighting Factor MPC

Fuzzy logic system is a powerful tool to approximate unknown continuous functions, and it has also been broadly utilized in the control of nonlinear systems [32], [33]. This article adopts fuzzy control as the strategy for variable weighting factors and proposes an FCMPC method, in which the motor operations are used as inputs to achieve dynamic adjustment of weighting coefficients under different operations. The overall structure of the fuzzy control strategy is shown in Fig. 5. The design procedure includes the following key steps.

1) Selection of Input Variable: Rotor speed ω_r and load torque T_L are chosen as the input variables of the fuzzy inference system.

2) Definition of Membership Functions: To construct the fuzzy inference system, the fuzzy universes of discourse for the input and output variables need to be defined. The load

TABLE II
OPTIMAL q_i RANGES UNDER DIFFERENT TORQUE AND SPEED CONDITIONS

$q_i(10^{-3})$		Speed / r/min								
		400	500	600	700	800	900	1000	1100	1200
Torque / N·m	0.5	[5,6]	[5,6]	[5,6]	[4,5]	[3,4]	[3,4]	[2,3]	[2,3]	[2,3]
	1.0	[5,6]	[5,6]	[5,6]	[5,6]	[5,6]	[5,6]	[5,6]	[5,6]	[5,6]
	1.5	[5,6]	[5,6]	[5,6]	[5,6]	[4,5]	[4,5]	[3,4]	[3,4]	[3,4]
	2.0	[4,5]	[4,5]	[4,5]	[4,5]	[3,4]	[3,4]	[2,3]	[2,3]	[2,3]
	2.5	[3,4]	[3,4]	[2,3]	[2,3]	[2,3]	[2,3]	[1,2]	[1,2]	[1,2]

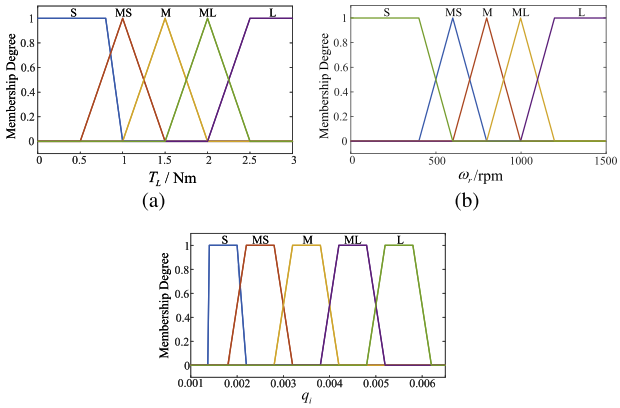

Fig. 6. Membership function diagram. (a) Load torque. (b) Motor speed. (c) Weighting coefficient.

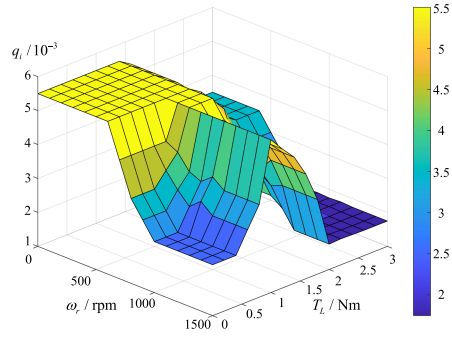

Fig. 7. Fuzzy surface of the weighting coefficient.

TABLE III
FUZZY RULE TABLE FOR q_i BASED ON ω_r AND T_L

q_i		ω_r				
		S	MS	M	ML	L
T_L	S	L	L	M	MS	MS
	MS	L	L	L	L	L
	M	L	L	L	ML	ML
	ML	ML	ML	M	MS	S
	L	M	MS	S	S	S

torque T_L is defined within the range [0N · m, 3N· m], the rotor speed ω_r within [0 r/min, 1500 r/min], and the current weighting factor q_i within [0.001, 0.007]. For each of these three variables, fuzzy subsets with consistent resolution are established, categorized as small, medium-small, medium, medium-large, and large, represented by the linguistic terms S, MS, M, ML, and L, respectively. The corresponding membership functions are illustrated in Fig. 6.

3) Rule Base Design: After the fuzzification of input and output signals, the fuzzy control rules are designed as follows: when both the motor load torque and speed are high, the current weighting factor q_i should be appropriately reduced; when the load torque is at a medium level, q_i should be increased to maintain effective current constraint; and when the load torque is low, q_i should be reduced as the speed increases. Based on the above analysis, the fuzzy rule base for the variable weighting MPC of the SRM is established, as shown in Table III.

4) Fuzzy Inference and Defuzzification: After the input values are fuzzified, they are mapped to the corresponding output fuzzy subsets based on the established fuzzy rules. The fuzzy inference engine combines the membership degrees of the input variables with the output subsets defined in the rules, and uses the Mamdani inference method [34] to deduce the output fuzzy region. The inference process is as follows:

$$F_{q_i} = (F_{T_L} \times F_{\omega_r}) \circ R = \bigcup_{i=1}^{25} (F_{T_L} \times F_{\omega_r}) \circ R_i. \quad (14)$$

Specifically, F_{qi} denotes the fuzzy set of the output current weighting factor, while F_{T_L} and $F_{\omega r}$ represent the fuzzy sets of the load torque and rotor speed, respectively. R_i corresponds to the ith fuzzy rule. The symbol "$\circ$" indicates the composition operation in fuzzy inference, which in this case refers to the max–min composition employed in the Mamdani method. In the expression, "$\times$" denotes the intersection operation, whereas "$\cup$" denotes the union operation.

After obtaining the output fuzzy set through fuzzy inference, the centroid method is used for defuzzification to obtain a precise numerical value for the output variable. The output surface of the current weighting factor defuzzified using the centroid method is illustrated in Fig. 7.

C. Design of Load Torque Observer

Load torque is one of the input variables to the fuzzy controller. Since it is difficult to measure directly in practical systems, a load torque observer is required to estimate it. The sliding-mode observer offers advantages, such as fast response, strong robustness, and low sensitivity to parameter variations [35]. In this section, a sliding-mode load torque observer is designed, which takes the electromagnetic torque and motor

speed as inputs to estimate the load torque. The estimated torque is then used as the torque input for the fuzzy controller.

The mechanical motion equation of the SRM is given by

$$\frac{d\omega}{dt} = \frac{T_{\text{em}}}{J} - \frac{T_L}{J} - \frac{D}{J}\omega. \tag{15}$$

Based on the sliding-mode control principle, the speed observation equation is constructed as follows:

$$\frac{d\hat{\omega}}{dt} = \frac{T_{\text{em}}}{J} - Z_s - \frac{D}{J}\omega. \tag{16}$$

Here, $\hat{\omega}$ is the estimated speed and $Z_s = k\,\text{sign}(\hat{\omega} - \omega)$ denotes the sliding-mode control law, where k is the sliding-mode gain.

By defining the speed estimation error, the sliding surface can be designed as

$$s(x) = \hat{\omega} - \omega. \tag{17}$$

By subtracting (8) from (7), we obtain

$$\frac{d\tilde{\omega}}{dt} = \frac{T_L}{J} - Z_s - \frac{D}{J}\hat{\omega}. \tag{18}$$

According to sliding-mode control theory, when the system reaches steady state and operates near the sliding surface, the speed observation equation approximates the actual speed state equation. Thus, the sliding surface satisfies $s(x) = \dot{s}(x) = 0$. Under this condition, the observed value of the motor load torque is given by

$$\hat{T}_L' = JZ_s. \tag{19}$$

To ensure the reachability and stability of sliding-mode control, the sliding surface must satisfy the condition: $s\dot{s} < 0$. Through analysis, it is determined that the sliding-mode gain k must satisfy

$$k > \frac{T_L - Ds}{J}. \tag{20}$$

Due to the discontinuity of the sliding-mode control law, the estimated load torque contains significant high-frequency switching components. To suppress this interference, a low-pass filter is introduced to eliminate the high-frequency noise. Therefore, the filtered estimated load torque can be expressed as

$$\hat{T}_L = JZ_s \cdot \frac{\omega_c}{s + \omega_c}. \tag{21}$$

D. Overall Architecture of the FCMPC Control System

The final structure of the sliding-mode load torque observer is illustrated in Fig. 8.

The control framework integrates several functional modules, including the PI controller, fuzzy logic module, predictive model, load torque observer, and power converter, and the arrows in Fig. 8 clearly illustrate the signal flow and parameter dependencies among them. Specifically, the PI speed controller generates the reference torque command T_{ref} based on the speed error. The fuzzy logic module receives the current speed and load torque information and outputs the adaptive weighting coefficient q_i for the cost function. The predictive model calculates the predicted torque and current values for each candidate switching

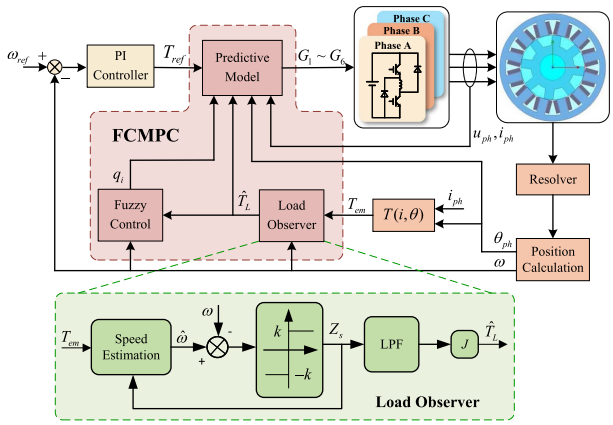

Fig. 8. FCMPC control block diagram.

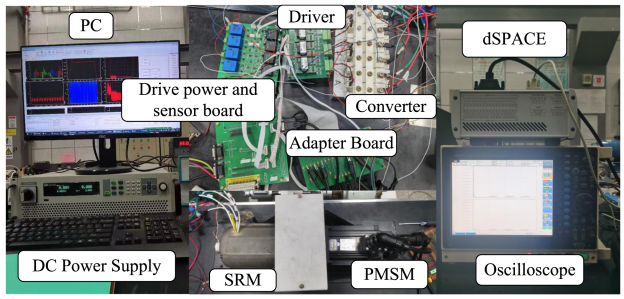

Fig. 9. Photograph of the employed experimental test bench.

TABLE IV
PROTOTYPE PARAMETERS OF THE 12/8-POLE SRM

Parameter	Value
Rated power	600 W
Rated speed	2000 r/min
Rated load torque	3 N·m
Rated current	20 A
Phase resistance	0.22 Ω
Friction coefficient	0.002 N·m·s
Moment of inertia	0.00095867 kg·m^2

state, while the sliding-mode observer estimates the load torque to enhance prediction accuracy. Finally, the controller selects the optimal switching state by minimizing the cost function and applies it to the power converter.

Compared with the conventional MPC method, the proposed FCMPC strategy flexibly allocates control priorities under different operating conditions, achieving faster dynamic response, lower torque ripple, and superior overall control performance.

IV. EXPERIMENTAL VERIFICATION

In this section, the proposed FCMPC method is experimentally verified and compared with the fixed-weight MPC method, in which the current weighting coefficient is fixed at $q_i = 0.006$. A photograph of the experimental test bench is shown in Fig. 9, where a three-phase 12/8-pole SRM is employed. The main parameters of the prototype are listed in Table IV.

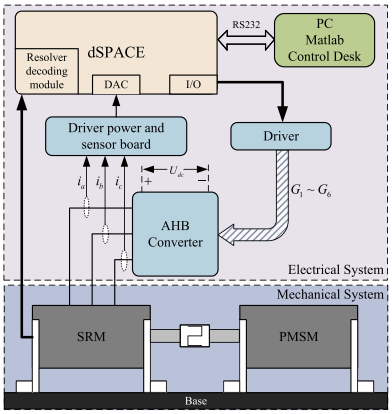

Fig. 10. Experimental setup and control architecture of the SRM drive system.

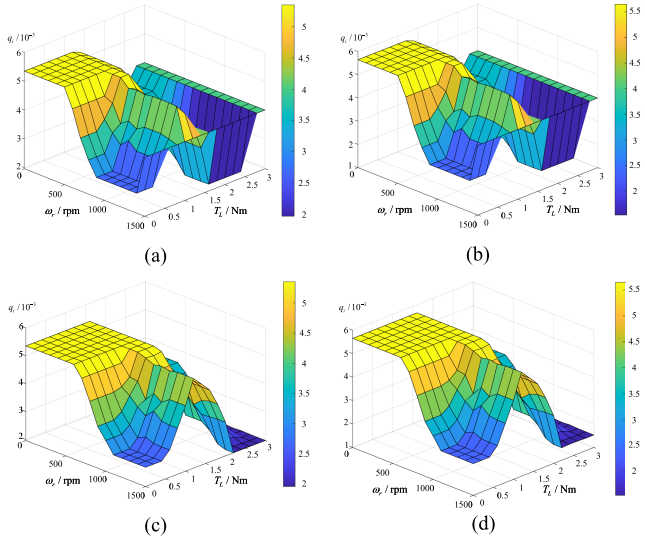

Fig. 11. Surfaces of weighting coefficient under membership-function perturbations. (a) Mode 1. (b) Mode 2. (c) Mode 3. (d) Mode 4.

The detailed hardware configuration and signal flow of the experimental platform are shown in Fig. 10. The system mainly consists of two parts: an electrical subsystem and a mechanical subsystem. Control commands are transmitted from the PC-MATLAB control desk to the dSPACE control system via an RS232 interface. The dSPACE unit outputs switching control signals to the driver through the I/O module, and the driver subsequently controls the converter switches G1–G6. The phase currents are measured by the sensor circuit and feedback to the dSPACE in real time. Meanwhile, the resolver decoding module provides rotor position and speed information to the control system.

In the experiment, both the control and sampling frequencies were set to 10 kHz, and the dc bus voltage was 96 V. The speed PI controller gains were chosen as $K_p = 0.2$ and $K_i = 0.08$. The cutoff frequency of the low-pass filter in the observer was set to $\omega_c = 12$, and the sliding-mode gain was selected as $k = 3000$. The experiments are organized into three parts: fuzzy parameter sensitivity analysis, dynamic performance evaluation, and steady-state performance verification.

A. Sensitivity Analysis of Fuzzy Parameters

The sensitivity of fuzzy parameter tuning was evaluated by proportionally perturbing the membership functions of the input and output variables by $\pm$ 10%, while keeping the rule base unchanged. As illustrated in Fig. 11, four configurations were considered: mode 1, both input and output membership functions reduced by 10%; mode 2, the input membership functions reduced and the output ones increased by 10%; mode 3, the input membership functions increased and the output ones reduced by 10%; and mode 4, both input and output membership functions increased by 10%. The baseline configuration without perturbation corresponds to the case shown previously in Fig. 11.

Table V presents the performance comparison under $\pm$ 10% membership-function perturbations at 1200 r/min and 2 N $\cdot$ m. Compared with the baseline condition, the efficiency variation among the four perturbation configurations is minimal, while The torque ripple increases moderately by about 0.21%–2.54%, indicating a minor tradeoff between smoothness and efficiency caused by variations in q_i. Overall, the proposed FCMPC method exhibits low sensitivity to membership-function perturbations.

TABLE V
PERFORMANCE RESULTS UNDER MEMBERSHIP PERTURBATIONS

Case	Torque Ripple	Efficiency	Weighting Coefficient
baseline	61.80%	70.59%	1.746×10^{-3}
mode 1	63.42%	71.42%	1.979×10^{-3}
mode 2	62.01%	70.32%	1.555×10^{-3}
mode 3	63.98%	71.78%	3.114×10^{-3}
mode 4	64.34%	71.55%	2.944×10^{-3}

B. Experimental Verification of Dynamic Performance

To analyze the dynamic performance of the proposed FCMPC method under transient conditions, both variable-speed and load-step experiments were conducted at low-, medium-, and high-speed operating conditions. All experiments were compared with the conventional MPC method with a fixed weighting coefficient of 0.006.

1) Variable-Speed Performance: The transient response of the proposed FCMPC method under varying speed conditions was examined through two acceleration experiments at a constant load torque of 2 N $\cdot$ m. In the first experiment, the motor speed was increased from 400 to 800 r/min, while in the second, it was raised from 800 to 1200 r/min.

Figs. 12 and 13 illustrate that both methods exhibit a slight overshoot during acceleration, with the FCMPC showing a slightly higher peak due to the fuzzy weighting mechanism, which emphasizes smoothness and vibration suppression at the initial transient stage. In contrast, the fixed-weight MPC shows larger current fluctuations and more significant torque oscillations as the speed increases. The adaptive weighting coefficient q_i in the FCMPC method can quickly respond to speed variations and stabilizes within about 0.3 s, effectively balancing

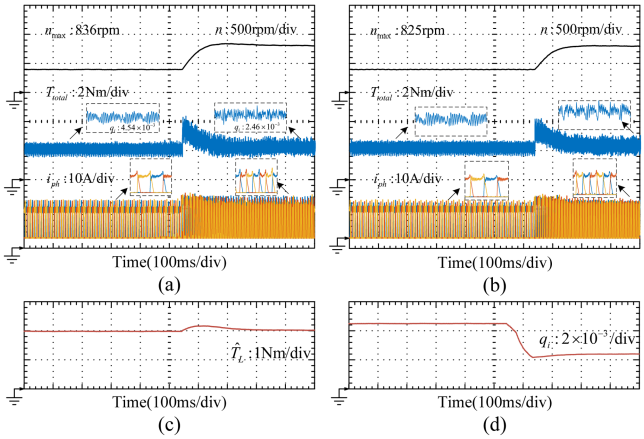

Fig. 12. Experimental results of the acceleration process from 400 to 800 r/min at 2 N · m. (a) Proposed FCMPC method. (b) Fixed-weight MPC method. (c) Observed load torque. (d) Adaptive weighting coefficient.

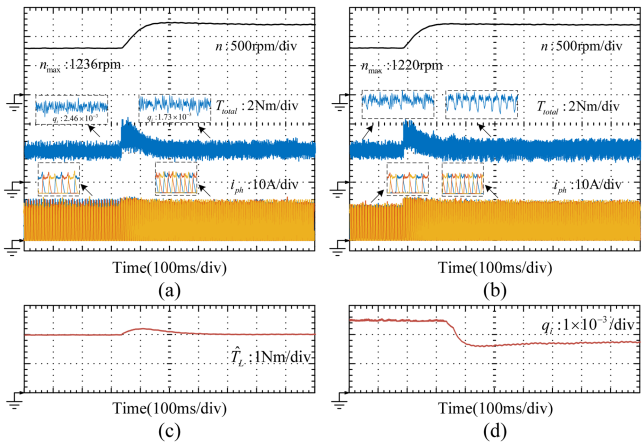

Fig. 13. Experimental results of the acceleration process from 800 to 1200 r/min at 2 N · m. (a) Proposed FCMPC method. (b) Fixed-weight MPC method. (c) Observed load torque. (d) Adaptive weighting coefficient.

smoothness and dynamic response. The results indicate that the proposed method can maintain stable torque output and high dynamic adaptability over a wide speed range.

2) Load-Step Performance: As shown in Figs. 14 –16, when the load torque suddenly changes from 1 to 2 N· m at constant speeds of 400 r/min, 800 r/min, and 1200 r/min, the proposed FCMPC method exhibits smaller torque ripple and smoother current response compared with the fixed-weight MPC method. The proposed controller adapts more effectively to the load variation process, allowing the system to stabilize rapidly at the new steady state. Throughout the load-step transient, the phase currents under FCMPC control remain continuous and stable, whereas those of the fixed-weight MPC display more noticeable fluctuations. Meanwhile, under all three operating conditions, the observed load torque accurately follows the actual variation, and the adaptive weighting coefficient q_i adjusts in real time according to the system state, achieving a balanced coordination between smoothness and dynamic response.

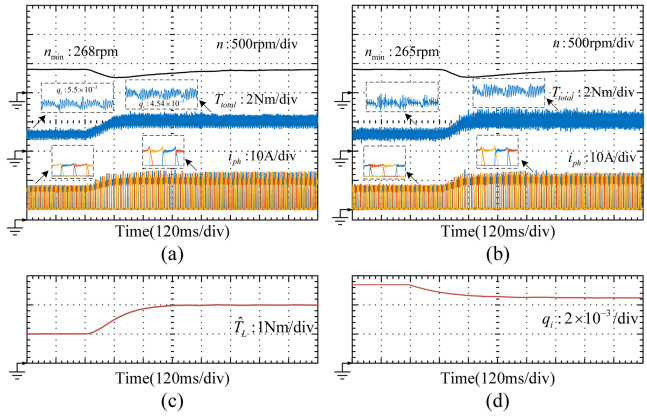

Fig. 14. Experimental result of the load-step from 1 to 2 N· m at 400 r/min. (a) Proposed FCMPC method. (b) Fixed-weight MPC method. (c) Observed load torque. (d) Adaptive weighting coefficient.

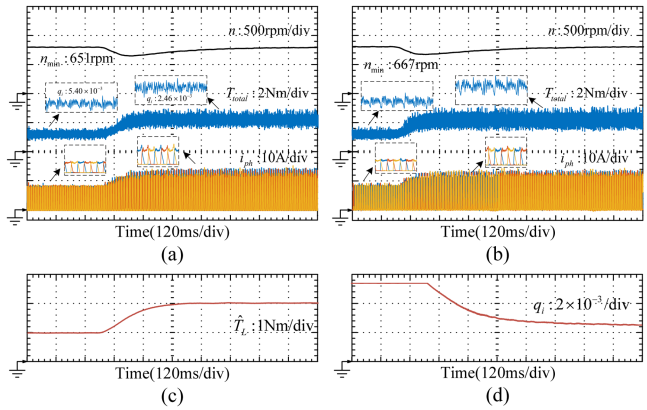

Fig. 15. Experimental result of the load-step from 1 to 2 N · m at 800 r/min. (a) Proposed FCMPC method. (b) Fixed-weight MPC method. (c) Observed load torque. (d) Adaptive weighting coefficient.

From the two sets of dynamic experiments, it can be concluded that the proposed FCMPC method can achieve fast response and smooth transition under various transient conditions, such as variable-speed operation and load disturbance. The fuzzy weighting adjustment mechanism adaptively optimizes the control parameters according to the operating state, while the load observer accurately estimates external disturbances, thereby significantly improving the system's dynamic performance.

C. Experimental Verification of Steady-State Performance

The steady-state control performance of the proposed FCMPC method was verified through comparative experiments conducted at three constant speeds: 400 r/min, 800 r/min, and 1200 r/min, under a fixed load torque of 2 N · m.

1) Low-Speed Steady-State Operation: Fig. 17(a) and (b) shows the steady-state total torque and phase current waveforms of the proposed FCMPC and fixed-weight MPC methods at 400 r/min and 2 N · m. Fig. 17(c) and (d) depicts the corresponding observed load torque and adaptive weighting coefficient, with average values of 1.9761 N· m and 4.5480 $\times 10^{-3}$, respectively.

TABLE VI
STEADY-STATE PERFORMANCE UNDER DIFFERENT SPEEDS AND LOADS

Method	400 r/min/ 1 N·m		400 r/min / 2 N·m		800 r/min / 1 N·m		800 r/min / 2 N·m		1200 r/min / 1 N·m		1200 r/min / 2 N·m	
	k_T	η	k_T	η	k_T	η	k_T	η	k_T	η	k_T	η
Fixed-weight MPC	0.7416	49.58%	0.5191	57.38%	0.7139	59.36%	0.6265	66.87%	0.7683	61.88%	0.7237	70.37%
FCMPC	0.6249	52.36%	0.4666	57.41%	0.6293	60.71%	0.5980	67.83%	0.7459	62.21%	0.6180	70.59%

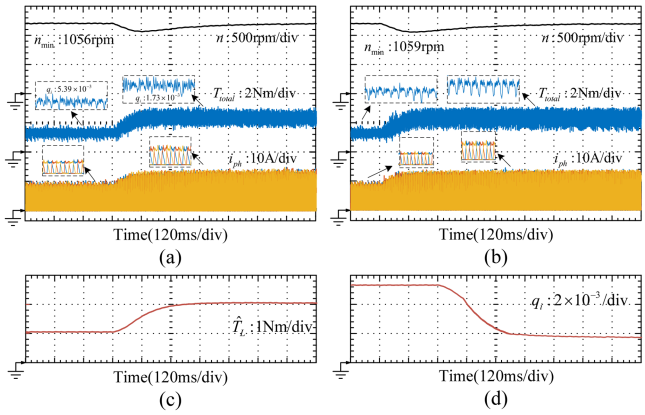

Fig. 16. Experimental result of the load-step from 1 to 2 N · m at 1200 r/min. (a) Proposed FCMPC method. (b) Fixed-weight MPC method. (c) Observed load torque. (d) Adaptive weighting coefficient.

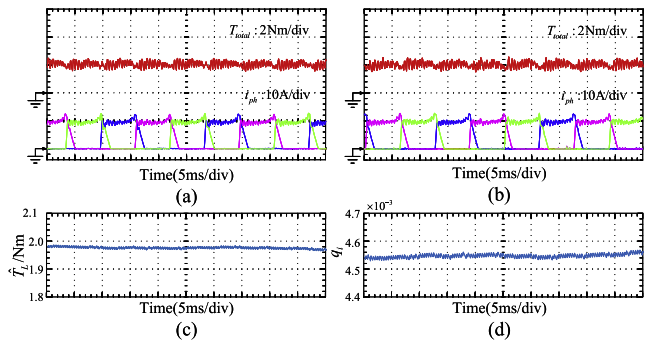

Fig. 17. Experimental steady-state results at 400 r/min and 2 N · m. (a) Proposed FCMPC method. (b) Fixed-weight MPC method. (c) Observed load torque. (d) Adaptive weighting coefficient.

2) Medium-Speed Steady-State Operation: Fig. 18(a) and (b) shows the steady-state total torque and phase current waveforms of the proposed FCMPC and fixed-weight MPC methods at 800 r/min and 2 N· m. The torque waveform under FCMPC control is noticeably smoother, benefiting from the adaptive weighting coefficient q_i that dynamically adjusts with operating conditions. Fig. 18(c) and (d) depicts the corresponding observed load torque and adaptive weighting coefficient, with average values of 2.0032 N· m and 2.4990 $\times 10^{-3}$, respectively.

3) High-Speed Steady-State Operation: Fig. 19(a) and (b) shows the steady-state total torque and phase current waveforms of the proposed FCMPC and fixed-weight MPC methods at 1200 r/min. At this higher speed, the torque waveform of the FCMPC is smoother, whereas the fixed-weight MPC exhibits larger oscillations and higher ripple amplitude. Fig. 19(c) and (d)

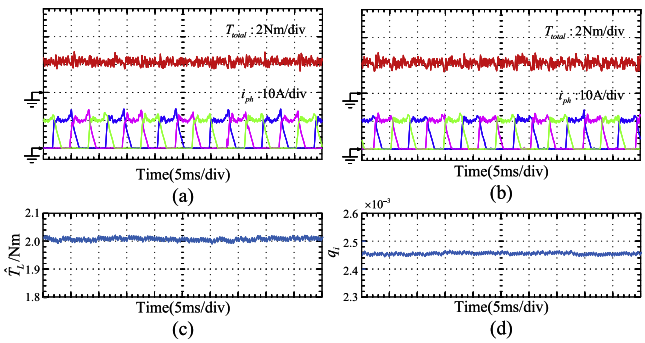

Fig. 18. Experimental steady-state results at 800 r/min and 2 N · m. (a) Proposed FCMPC method. (b) Fixed-weight MPC method. (c) Observed load torque. (d) Adaptive weighting coefficient.

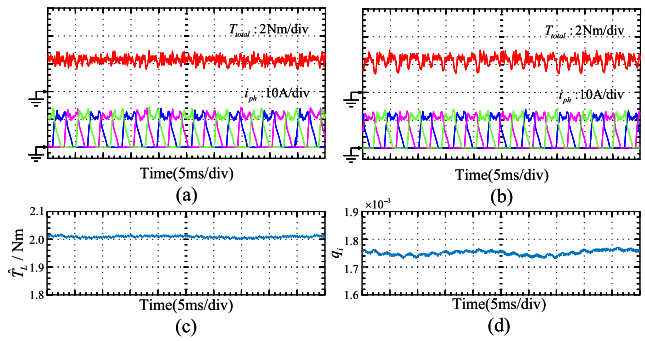

Fig. 19. Experimental steady-state results at 1200 r/min and 2 N · m. (a) Proposed FCMPC method. (b) Fixed-weight MPC method. (c) Observed load torque. (d) Adaptive weighting coefficient.

presents the corresponding observed load torque and adaptive weighting coefficient, with average values of 2.0238 N· m and 1.7467 $\times 10^{-3}$, respectively.

To further verify the general applicability of the proposed method, steady-state experiments were conducted at low, medium, and high speeds under a load torque of 1 N · m. For quantitative analysis, Table VI summarizes the torque ripple and efficiency results under different speed and load conditions. It can be observed that the proposed FCMPC method achieves lower torque ripple under all operating conditions, showing a clear advantage over the fixed-weight MPC. Meanwhile, the overall efficiencies of the two methods remain nearly the same, indicating that the proposed method improves torque smoothness without sacrificing system efficiency. The experimental results demonstrate that the FCMPC provides more stable and balanced steady-state control performance, exhibiting strong adaptability to varying operating conditions and great potential for high-performance SRM drive applications.

Finally, to compare the computational burden of the two methods, the single-cycle execution time was measured using the dSPACE turnaround module at a control frequency of 10 kHz. Under the condition of 1200 r/min and 2 N · m, the average execution times of the fixed-weight MPC and the proposed FCMPC method were 29.3 μs and 29.7 μs, respectively, with an increase of only 0.4 μs, accounting for about 1.4% of one sampling period. This result indicates that the computational overhead introduced by the fuzzy weighting module is negligible, since the main computational burden of MPC arises from the prediction and cost evaluation of candidate switching states, which are identical in both methods.

V. Conclusion

This article proposes an FCMPC strategy aimed at reducing torque ripple in SRMs and extending their application to high-precision servo control. By integrating a load torque observer with fuzzy logic, the proposed method enables real-time adjustment of the weighting coefficients in the MPC cost function according to operating conditions. Experimental evaluations under various combinations of speeds and loads demonstrate that the proposed FCMPC strategy outperforms conventional MPC with fixed weighting coefficients in torque ripple suppression and efficiency improvement, exhibiting excellent dynamic and steady-state performance as well as strong adaptability under different operating conditions. These findings confirm the superior robustness and effectiveness of the proposed method in achieving adaptive priority control and enhancing overall SRM performance, providing a promising solution for high-performance control under complex operating conditions.

References

[1] K. U. Ehigiamusoe, M. Shahbaz, and X. V. Vo, "How does globalization influence the impact of tourism on carbon emissions and ecological footprint? Evidence from African countries," *J. Travel Res.*, vol. 62, no. 5, pp. 1010–1032, 2023.

[2] S. Speizer et al., "Integrated assessment modeling of a zero-emissions global transportation sector," *Nature Commun.*, vol. 15, no. 1, 2024, Art. no. 4439.

[3] G. Buticchi, P. Wheeler, and D. Boroyevich, "The more-electric aircraft and beyond," *Proc. IEEE*, vol. 111, no. 4, pp. 356–370, Apr. 2023.

[4] J. Z. Bird, "A review of electric aircraft drivetrain motor technology," *IEEE Trans. Magn.*, vol. 58, no. 2, Feb. 2022, Art. no. 8201108.

[5] R. Bojoi, A. Cavagnino, A. Tenconi, and S. Vaschetto, "Control of shaft-line-embedded multiphase starter/generator for aero-engine," *IEEE Trans. Ind. Electron.*, vol. 63, no. 1, pp. 641–652, Jan. 2016.

[6] J. Benzaquen, J. He, and B. Mirafzal, "Toward more electric powertrains in aircraft: Technical challenges and advancements," *CES Trans. Elect. Mach. Syst.*, vol. 5, no. 3, pp. 177–193, 2021.

[7] H. Chen et al., "Reliability analysis of a switched reluctance starter/generator," *Protection Control Modern Power Syst.*, vol. 9, no. 1, pp. 112–121, 2024.

[8] V. K. Singh, B. Singh, and J. Gupta, "Totem pole dual output bridgeless rectifier for high-performance low power SRM drive," *IEEE Trans. Power Electron.*, vol. 40, no. 11, pp. 16498–16511, Nov. 2025.

[9] M. A. Prabhu et al., "Magnetic loading of soft magnetic material selection implications for embedded machines in more electric engines," *IEEE Trans. Magn.*, vol. 52, no. 5, May 2016, Art. no. 2002206.

[10] L. Ge, J. Zhong, C. Bao, S. Song, and R. W. De Doncker, "Continuous rotor position estimation for SRM based on transformed unsaturated inductance characteristic," *IEEE Trans. Power Electron.*, vol. 37, no. 1, pp. 37–41, Jan. 2022.

[11] S. Xu, F. Song, G. Qi, G. Han, and C. Liu, "Switch fault diagnosis for switched reluctance motors based on current double-measurement," *IEEE Trans. Power Electron.*, vol. 40, no. 4, pp. 6010–6019, Apr. 2025.

[12] G. Sun, S. Song, J. Jiang, L. Ge, and W. Liu, "Characteristics testing and torque control of aero-engine shaft-line-embedded switched reluctance starter/generator," *IEEE Trans. Ind. Appl.*, vol. 59, no. 6, pp. 7295–7305, Nov./Dec. 2023.

[13] L. Ge, J. Zhong, J. Huang, N. Jiao, S. Song, and R. W. De Doncker, "A novel model predictive torque control of SRMs with low measurement effort," *IEEE Trans. Ind. Electron.*, vol. 70, no. 4, pp. 3561–3570, Apr. 2023.

[14] S. Song, R. Hei, R. Ma, and W. Liu, "Model predictive control of switched reluctance starter/generator with torque sharing and compensation," *IEEE Trans. Transport. Electrific.*, vol. 6, no. 4, pp. 1519–1527, Dec. 2020.

[15] L. Ge et al., "Advanced technology of switched reluctance machines in more electric aircraft: A review," *IEEE Trans. Power Electron.*, vol. 40, no. 1, pp. 195–216, Jan. 2025.

[16] G. Fang, F. P. Scalcon, D. Xiao, R. P. Vieira, H. A. Gründling, and A. Emadi, "Advanced control of switched reluctance motors (SRMs): A review on current regulation, torque control and vibration suppression," *IEEE Open J. Ind. Electron. Soc.*, vol. 2, pp. 280–301, 2021.

[17] S. Song et al., "A harmonic optimized deadbeat predictive control method for switched reluctance machine," *IEEE Trans. Power Electron.*, vol. 41, no. 2, pp. 2171–2180, Feb. 2026.

[18] J. Cai, X. Dou, A. D. Cheok, W. Ding, Y. Yan, and X. Zhang, "Model predictive control strategies in switched reluctance motor drives—an overview," *IEEE Trans. Power Electron.*, vol. 40, no. 1, pp. 1669–1685, Jan. 2025.

[19] C. Sun, X. Sun, C. Garcia, J. Rodriguez, Z. Yang, and S. Han, "Model predictive current control of six-phase switched reluctance motor with enhanced robustness based on improved Lehuy model," *IEEE Trans. Transport. Electrific.*, vol. 11, no. 2, pp. 6177–6187, Apr. 2025.

[20] L. Ge, J. Guo, C. Gong, G. Zhang, X. Ding, and S. Song, "Model predictive torque control of switched reluctance machines with torque sharing function and PWM control signals based on linear polynomial fitting," *IEEE Trans. Power Electron.*, vol. 40, no. 1, pp. 40–45, Jan. 2025.

[21] G. Han, H. Zhu, L. Zhang, J. Hong, and B. Zhu, "Model-free current predictive control method for switched reluctance motors," *IEEE Trans. Ind. Electron.*, vol. 71, no. 10, pp. 12041–12050, Oct. 2024.

[22] I. Harbi et al., "Model-predictive control of multilevel inverters: Challenges, recent advances, and trends," *IEEE Trans. Power Electron.*, vol. 38, no. 9, pp. 10845–10868, Sep. 2023.

[23] M. F. Elmorshedy, W. Xu, S. M. Allam, J. Rodriguez, and C. Garcia, "MTPA-based finite-set model predictive control without weighting factors for linear induction machine," *IEEE Trans. Ind. Electron.*, vol. 68, no. 3, pp. 2034–2047, Mar. 2021.

[24] S. Wang, F. Jiang, Y. Guo, and S. Cheng, "Multi-objective model predictive control with weighting factor elimination for PMSM drives," *IEEE Trans. Transport. Electrific.*, vol. 11, no. 6, pp. 12805–12817, Dec. 2025.

[25] H. Xie et al., "Cooperative decision-making approach for multiobjective finite control set model predictive control without weighting parameters," *IEEE Trans. Ind. Electron.*, vol. 71, no. 5, pp. 4495–4506, May 2024.

[26] X. Zhang and Y. He, "Direct voltage-selection based model predictive direct speed control for PMSM drives without weighting factor," *IEEE Trans. Power Electron.*, vol. 34, no. 8, pp. 7838–7851, Aug. 2019.

[27] F. Wang et al., "Design of model predictive control weighting factors for PMSM using Gaussian distribution-based particle swarm optimization," *IEEE Trans. Ind. Electron.*, vol. 69, no. 11, pp. 10935–10946, Nov. 2022.

[28] C. Yao, Z. Sun, S. Xu, H. Zhang, G. Ren, and G. Ma, "ANN optimization of weighting factors using genetic algorithm for model predictive control of PMSM drives," *IEEE Trans. Ind. Appl.*, vol. 58, no. 6, pp. 7346–7362, Nov./Dec. 2022.

[29] P. R. U. Guazzelli, W. C. de Andrade Pereira, C. M. R. de Oliveira, A. G. de Castro, and M. L. de Aguiar, "Weighting factors optimization of predictive torque control of induction motor by multiobjective genetic algorithm," *IEEE Trans. Power Electron.*, vol. 34, no. 7, pp. 6628–6638, Jul. 2019.

[30] X. Liu, J. Wang, X. Gao, W. Tian, L. Zhou, and R. Kennel, "Robust predictive speed control of SPMSM drives with algebraically designed weighting factors," *IEEE Trans. Power Electron.*, vol. 37, no. 12, pp. 14434–14446, Dec. 2022.

[31] R. Yuan et al., "A method of torque ripple suppression of SRM based on model predictive control," in *Proc. IEEE Int. Conf. Predictive Control Elect. Drives Power Electron.*, 2021, pp. 229–234.

[32] F. Tang, B. Niu, H. Wang, L. Zhang, and X. Zhao, "Adaptive fuzzy tracking control of switched MIMO nonlinear systems with full state constraints and unknown control directions," *IEEE Trans. Circuits Syst. II: Exp. Briefs*, vol. 69, no. 6, pp. 2912–2916, Jun. 2022.
[33] Y. Li, Y. Liu, and S. Tong, "Observer-based neuro-adaptive optimized control of strict-feedback nonlinear systems with state constraints," *IEEE Trans. Neural Netw. Learn. Syst.*, vol. 33, no. 7, pp. 3131–3145, Jul. 2022.
[34] A. Nanda and A. K. Rath, "Mamdani fuzzy inference based hierarchical cost effective routing (MFIHR) in WSNs," in *Proc. IEEE 7th Int. Adv. Comput. Conf.*, 2017, pp. 397–401.
[35] W. Xu, S. Qu, L. Zhao, and H. Zhang, "An improved adaptive sliding mode observer for middle-and high-speed rotor tracking," *IEEE Trans. Power Electron.*, vol. 36, no. 1, pp. 1043–1053, Jan. 2021.

Shoujun Song (Senior Member, IEEE) received the B.S. and M.S. degrees from Northwestern Polytechnical University, Xi'an, China, in 2003 and 2006, respectively, and the Dr.-Ing. degree from the Technical University of Berlin, Berlin, Germany, in 2009, all in electrical engineering.

He is currently a Professor with the School of Automation, Northwestern Polytechnical University. His research interests include electric machines and drives in more electric aircraft with an emphasis on switched reluctance machines and permanent magnet machines.

Dr. Song is currently an Associate Editor for the IEEE TRANSACTIONS ON INDUSTRIAL ELECTRONICSand IEEE TRANSACTIONS ON TRANSPORTATION ELECTRIFICATION.He was the Recipient of the 2018 and 2019 Best Paper Awards from the International Conference on Electrical Machines and Systems.

Xinyu Bai was born in China, in 2002. She received the B.S. degree in electrical engineering from Chang'an University, Xi'an, China, in 2024. She is currently working toward the M.S. degree in electrical engineering with Northwestern Polytechnical University, Xi'an, China.

Her research interests include electrical machines and drives with emphasis on the advanced control of switched reluctance machines.

Guilin Sun was born in Sichuan, China. He received the B.S. degree in electrical engineering from the Shenyang University of Technology, Shenyang, China, in 2018, and the M.S. degree in electrical engineering from Northwestern Polytechnical University, Xi'an, China, in 2021, where he is currently working toward the Ph.D. degree in electrical engineering with the Department of Electrical Engineering.

His research interests include sensorless control of SRMs and shaft-line-embedded starter/generator in aviation.

Chaoyang Liu was born in China in 1999. He received the B.S. degree in electrical engineering and automation and the M.S. degree in power engineering from Northwestern Polytechnical University, Xi'an, China, in 2021 and 2024, respectively.

He focuses on the control of switched reluctance machines, with particular emphasis on model predictive control. He is currently an Electrical Components Engineer with the Platform and Module Development Department, Changan Automobile, Chongqing, China.

Lefei Ge (Member, IEEE)was born in China, in 1992. He received the B.S. degree in measurement and control technology and the M.S. degree in electrical engineering from Northwestern Polytechnical University, Xi'an, China, in 2013 and 2016, respectively, and the Dr.-Ing. degree in electrical engineering from RWTH Aachen University, Aachen, Germany, in 2020.

In September 2016, he became a Research Associate with the Institute of Power Electronics and Electrical Drives, RWTH Aachen University, Aachen, Germany. Since 2020, he has been an Associate Professor with the Department of Electrical Engineering, Northwestern Polytechnical University. His research interests include electrical machines and drives with emphasis on switched reluctance machines.

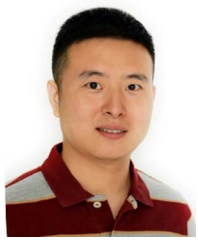

Ningfei Jiao (Member, IEEE) received the B.S. and Ph.D. degrees in electrical engineering from Northwestern Polytechnical University, Xi'an, China, in 2011 and 2017, respectively.

From 2013 to 2014, he was a Visiting Scholar with the Michigan Power and Energy Laboratory, University of Michigan, Ann Arbor, MI, USA. He is currently an Associate Research Professor with Northwestern Polytechnical University. His research interests include design, analysis, and control of integrated starter-generator and permanent magnet synchronous machines.

Weiguo Liu (Senior Member, IEEE) received the B.S. degree in electrical machine engineering from the Huazhong University of Science and Technology, Wuhan, China, in 1982, and the M.S. degree in electrical engineering and the Ph.D. degree in control theory and control engineering from Northwestern Polytechnical University, Xi'an, China, in 1988 and 1999, respectively.

He is currently a Professor with the School of Automation, Northwestern Polytechnical University. His research interests include brushless dc machines, PM synchronous machines, and induction machines.